Chandran, Aravind Ramesh; Hennen, Martin D.; Arkkio, Antero; Belahcen, Anouar

Safe Turn-off Strategy for Electric Drives in Automotive Applications

Published in:
IEEE Transactions on Transportation Electrification

DOI:
10.1109/TTE.2021.3104461

Published: 01/03/2022

Document Version
Publisher's PDF, also known as Version of record

Safe Turn-Off Strategy for Electric Drives in Automotive Applications

Aravind Ramesh Chandran, Martin D. Hennen, Antero Arkkio, and Anouar Belahcen, *Senior Member, IEEE*

***Abstract*— This article proposes a strategy to safely turn-off an electric drive system in case of a fault without destroying the power module and the electric machine. Classic turn-off strategies, such as active short circuit (ASC) and freewheeling (FW), are adopted as state of the art for electric vehicle applications. However, these methods cause either high currents in the machine or overvoltage in the dc-link capacitor, the system should be designed to withstand these unwanted effects making them more expensive. The novel method proposed in this study mitigates both overvoltage and overcurrents, thereby achieving a smooth transition from torque control to a safe state. The proposed method can be implemented almost cost neutral with respect to the state-of-the-art methods. In this method, voltage vectors are identified with respect to the position of the current vector, which can either charge or discharge the dc-link capacitor, hence keeping both the dc-link voltage and stator currents to a safe value. The proposed strategy is analyzed through simulations with a combined inverter and machine model. The simulation model includes skin effect loss models that are essential for the accurate calculation of the dc-link voltage. Measurements were done on an electric drive system to validate the strategy.**

***Index Terms*— DC-link capacitor, E-mobility, electric traction system, induction machines, overvoltage protection, power electronics.**

Nomenclature

δ	Skins depth.
ρ	Resistivity.
f	Frequency of the current.
μ_0	Permeability of free space.
ω_m	Angular speed of rotor.
ψ_M	Main flux linkage.
ψ_R	Rotor flux linkage.
ψ_S	Stator flux linkage.
$\text{Eoff}_{\text{diode}}$	Energy consumed during turn-off for a diode.
$\text{Eoff}_{\text{igbt}}$	Energy consumed during turn-off for an IGBT.
Eon_{igbt}	Energy consumed during turn-on for an IGBT.
E_{cap}	Energy stored in the capacitor.
E_{induLeak}	Energy stored in the leakage inductance.
E_{res}	Energy dissipated as ohmic losses in the machine.
i_μ	Magnetizing current.
i_{pm}	Current power module.
i_s	Stator current space vector.
K_r	Skin effect correction factor for rotor resistance.
K_x	Skin effect correction factor for rotor resistance.
L_M	Main inductance.
P_{cond}	Power module conduction losses.
P_{switch}	Power module switching losses.
R_{ac}	Skin effect correction factor for rotor resistance.
R_R	Rotor winding resistance.
R_S	Stator winding resistance.
si_x	Output from the comparator $x = 1, 2$, and 3.
S_x	Switching vector for phase $x = a, b$, and c.
u_α	Stator phase voltage in alpha axis.
u_β	Stator phase voltage in beta axis.
U_{ce}	Collector emittor voltage of the IGBT.
u_{dc}	DC-link voltage.
u_d	Phase voltage in direct axis.
U_{fw}	Forward voltage of the diode.
u_q	Phase voltage in quadrature axis.
u_S	Stator voltage space vector.
u_{xn}	Stator phase voltage (referred to the star point) $x = a, b$, and c.

Manuscript received December 5, 2020; revised March 30, 2021 and June 5, 2021; accepted July 13, 2021. Date of publication August 12, 2021; date of current version March 22, 2022. This work was supported by Robert Bosch Gmbh, Stuttgart. *(Corresponding author: Aravind Ramesh Chandran.)*

Aravind Ramesh Chandran, Antero Arkkio, and Anouar Belahcen are with the Department of Electrical Engineering and Automation, Aalto University, 02150 Espoo, Finland (e-mail: aravind.rameshchandran@aalto.fi).

Martin D. Hennen is with Robert Bosch Gmbh, 70442 Stuttgart, Germany.

Digital Object Identifier 10.1109/TTE.2021.3104461

I. Introduction

THE automobile industry throughout the world has been pushing for the electric propelled traction system in favor of the conventional internal combustion engines. The race for dominance in the electric mobility market has been highest ever than before, and every automobile maker and supplier has been urged to develop better electric drive systems that are more robust and power-dense. One of the most critical factors in designing an electric drive system in an automotive system is safety. Adhering to the high safety standards will require the system to turn-off from the active state to a final state with minimum stress on the components. In the event of a fault in an electric drive system or in an event where the electric drive system needs to be manually turned off, the system will go to a safe state. During the safe state, the energy exchange between the battery and the electric machine is interrupted so that no unwanted torque is generated, which would harm the driver or the passenger in the vehicle. Safe states are requested either as a reaction from a fault, which needs to be executed within a specified time, or it can also be a reaction to an explicit request from the vehicle control unit, which requests the motor controller to shut down. In prior art, there are mainly two classical safe state strategies.

The first method is active short circuit (ASC), which refers to actively short circuiting the windings of the machine using the inverter. Welchko *et al.* [1] have shown that in the event of a single-phase fault in the electric machine, short circuiting the three phases would reduce the post-fault currents and torque in the electric machine. The second method is to turn-off the gate supply of the inverter switches so that the machine behaves like an uncontrolled generator [2], [3]. This safe state is referred to as freewheeling (FW) in this article since the current would still continue to freewheel through the diodes till zero crossing. This second method generates lower post-fault stator currents and torque in the machine compared to the short circuiting method but generates a high overvoltage on the dc-link side. The impact on the dc-link capacitor for an induction machine drive is investigated in [4]. In [5], both the short- and open-circuit strategies are compared and evaluated in case of a single-phase open-circuit fault in the electric machine. Lu *et al.* [6] proposed a hybrid approach by varying the switching signals between FW and ASC. The selection of the safe state depends on the operating point of the electric machine and the type of electric machine used. A detailed explanation of these safe states is explained in Section II. The abrupt transition to any of the two mentioned safe states would always result in either a transient overcurrent in the electric machine or a transient voltage peak in the dc-link capacitor. Alternatively, if the request for safe state transition is not time critical, there are so-called soft turn-off strategies, which uses the main microcontroller of the inverter to slowly transition to either ASC or FW. For example, if the turn-off is predetermined or expected, the phase currents can be controlled down to zero and then safely turned off to a safe state. There are also different variations of soft turn-offs, especially soft-ASC where the reference U_d and U_q values can be ramped down to zero, which is a form of ASC. These methods are patented and can be found in [7]. Discharging the dc-link capacitor voltage by controlling the operating mode of the electric machine has also been discussed in [8]. Such soft transition techniques still require the main microcontroller of the inverter remain functional.

This article proposes a new safe state transition technique that employs specific voltage vectors depending on the current space vector, which transfers the inductive energy from the machine inductance to the dc-link capacitor or vice-versa. This energy transfer is accomplished in a manner that neither dc-link voltage nor the phase currents never crosses any values that would damage the system. This technique would be implemented on a hardware close complex programmable logical device (CPLD) that is more robust and fast to respond than the main microcontroller. A similar idea had already been discussed in [9] for a permanent magnet machine, and this article extends this idea of using charging (CV) and discharging (DV) vectors to turn-off a 90-kW induction machine drive in case of a fault. Some of the major differences and similarities to the article [9] have been listed in the following.

1) Both the work [9] and this article are trying to solve the same problem of overvoltage in the dc-link capacitor during an uncontrolled generation scenario. The work [9] is aiming to solve the problem for an electric drive with a permanent magnet synchronous machine, while in this article induction machine is in focus. The difference in the considered electric machine also changes where the energy is consumed during the strategy, and for the work [9], the energy transferred from the dc-link capacitor is burned in the stator windings of the permanent magnet machine. In this article, the rotor windings are the primary consumer of energy transferred from the dc-link capacitor.
2) In this article, the proposed method not only stops the dc-link voltage from rising any further but it has also the ability to discharge the dc-link voltage to a value of less than 60 V with a time of around 100 ms (also seen in the measurements, see Fig. 20). The reason is that mostly in an induction machine, the rotor flux linkage slowly dies out as the current also dies out in both the stator and rotor of the machine, while in [9], the primary goal was to halt the rising dc-link voltage but not to decrease it below 60 V.
3) In both [9] and this article, the idea of using the charging and discharging vectors is the same. The patterns or the distribution in which they are used are different, and the voltage vectors are optimized for an induction machine.

The strategy in detail and the hardware implementation are explained in Sections III and IV, respectively.

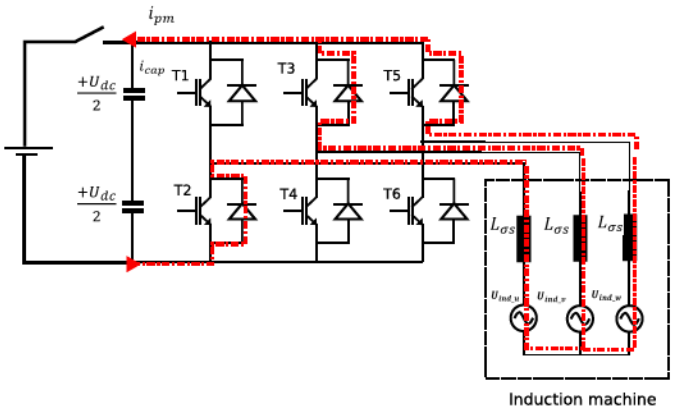

Fig. 1. Battery disconnection during generating.

II. Classical Safe State During Uncontrolled Generation

Fig. 1 shows a schematic of a three-phase electric drive system consisting of an electric machine, three-phase inverter, dc-link capacitor, and the battery. The three-phase inverter provides the necessary voltage to the electric machine, to achieve the desired torque. There is also a relay or a connector between the dc-link capacitor and the battery as shown in the figure. In case of a system failure such as overvoltage or overcurrent in the dc side, this connector is opened and the battery is isolated from the inverter machine side. The battery disconnection unit is usually activated in the event of a crash, and in this scenario, the dc-link capacitor voltage is supposed to decrease to a safe value of 60 V within 5 s to avoid any electrical shock risks as described in the United Nation Vehicle Regulation ECE R94 [10]. If the machine is in the regenerating mode, the current i_{pm} would flow entirely into

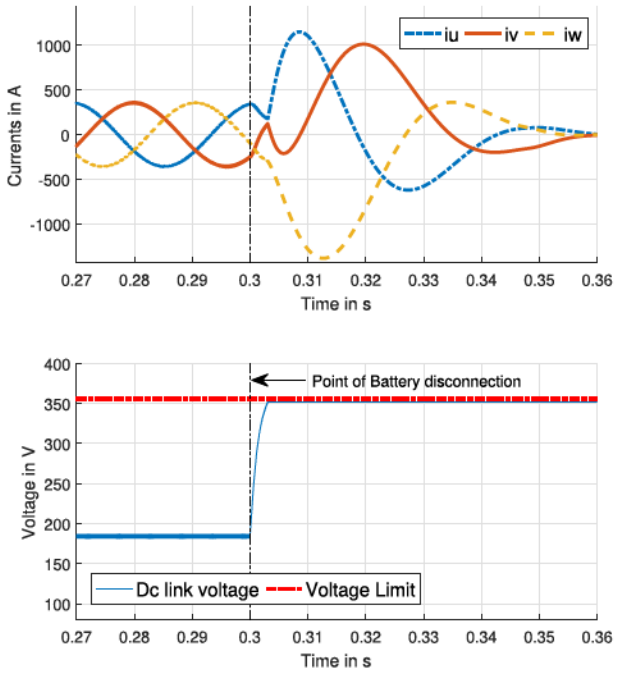

Fig. 2. High currents during ASC.

the dc-link capacitor. This creates a condition of uncontrolled dc-link voltage rise; the typical rate of voltage rise for the 90-kW induction machine considered in this article is around 2 V/μs. By the time the main microcontroller realizes that there is an overvoltage in the dc-link capacitor, the voltage in the dc-link capacitor would have already crossed the threshold and damaged the inverter. In this scenario, the only alternative reaction possible is to either go into ASC or FW, and this action is usually implemented on a CPLD chip, which acts swiftly and commands the inverter to go into the safe state.

A. Active Short Circuit

ASC refers to the intentional action of shorting the input phases of an electric machine to reach a desired safe state. Fig. 2 shows the simulation result for a 90-kW induction machine during ASC. In the simulation, the electric machine is initially ($t < 0.3$) in a generating operating point (1000 r/min and -100 Nm) with a stator current of 300 A (rms). At $t = 0.3$ s, the battery is disconnected creating a condition of uncontrolled generation, hence making the dc-link voltage to rise. A threshold of 355 V is set for the dc-link voltage after which ASC is triggered. ASC is achieved by commanding either the upper three or lower three insulated gate bipolar transistors (IGBTs) to be turned on, making a short circuit between the phases of the machine. This creates high transient currents in the machine and would eventually settle down to zero, as soon as the flux in the rotor of the induction motor decays. Nevertheless, the dc-link voltage remains constant after the threshold and is isolated from the electric machine. The maximum transient peak current during ASC for the simulated operating point is 1390 A, and this current increases with operating points with higher torque. The high stator current would destroy the inverter, and hence, ASC is not the preferred safe state for induction machines.

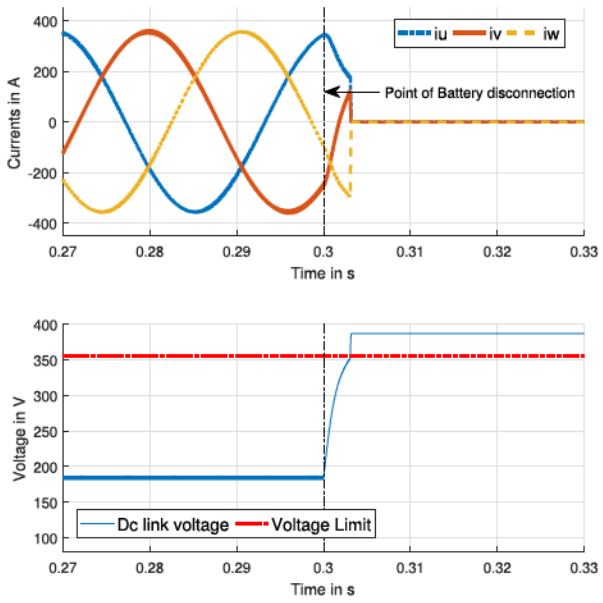

Fig. 3. DC-link capacitor overvoltage due to FW.

B. Freewheeling

Another alternative strategy is to directly turn-off all the switches in the inverter during a fault. When all the switches in the inverter are turned off, the currents in the machine continue to flow back to the dc-link capacitor through the FW diodes until the current commutates at zero crossing. The detailed analysis is done in [4].

Fig. 3 shows the simulation of an induction machine drive when a transition from normal torque control to FW occurs. As in the case of ASC, the electric machine is initially ($t < 0.3$) in a generating operating mode. At $t = 0.3$ s, the battery is disconnected creating a condition of uncontrolled generation, hence making the dc-link voltage to rise. A threshold of 355 V is set for the dc-link voltage after which FW is triggered. All the switches of the inverter are turned off, and this forces the current to flow back to the dc-link capacitor until current zero crossing. This increases the dc-link voltage further to 390 V and afterward remains constant.

Using ASC to turn-off the system prevents any transient voltage peaks in the dc-link capacitor; however, it causes high currents to flow through the phases (Fig. 2), demanding high current rating of the switching devices. FW can avoid these high currents but leads to a high transient voltage peak in the system (Fig. 3). However, the amplitude of this transient peak can be reduced by using a big dc-link capacitor or by choosing a high-voltage rating switching device that can withstand the transient peak. Such overdimensioning to cover these side effects will lead to higher cost of the system.

Almost all the disadvantages from ASC and FW can be solved using soft transitioning strategies, provided that the motive is to shut down the system slowly and time is not a critical factor. An uncontrolled generation scenario with battery relay open creates a rising voltage with a slew rate of slope 2 V/μs. If an action must be taken before the inverter is damaged, a faster response is required from the controller. In this scenario, the only alternative reaction possible today is to either go into ASC or FW, and this action is usually

implemented on a CPLD chip, which acts swiftly and commands the inverter to go into the post-fault state. In case the primary supply to the main controller fails, the CPLD chip and the gate driver circuits are provided with a redundant power supply that could still run during a fault situation. A new turn-off strategy is proposed in this article, which can also be triggered from a CPLD, but with no overcurrent or overvoltage.

III. Description of the Proposed Strategy

At any given operating point of an electric machine, there is always some energy stored in the inductance of the machine. This energy can be manipulated to charge or discharge the energy in the dc-link capacitor. In order to understand this, let us start with the basic equations of an induction machine.

A. Mathematical Model for an Induction Machine

The relationship between the stator phase currents and the applied voltage from the inverter can be explained by starting with the space vector model for an induction machine. An ideal rotating transformer (IRTF) machine model for an induction machine in the stator reference frame is taken as basis for our analysis [11]. The equations are explained with the following variables.

1) u_S is the stator voltage vector.
2) i_S and i_R are the stator current and rotor current vector, respectively.
3) R_S and R_R are the stator winding resistance and rotor resistance, respectively.
4) ψ_S, ψ_M, and ψ_R are the stator flux linkage, main flux linkage, and the rotor flux linkage respectively.
5) $L_{\sigma S}$ and $L_{\sigma R}$ are the stator leakage inductance and rotor leakage inductance, respectively.
6) L_M is the main inductance of the machine.
7) i_μ is the magnetizing current of the machine.

The voltage equations on the stator side are given as follows:

$$u_S = R_S i_S + \frac{d\psi_S}{dt},\ \psi_S = \psi_M + L_{\sigma S} i_S. \tag{1}$$

The main flux linkage formulations based on the magnetizing current are given as follows:

$$i_\mu = \frac{\psi_M}{L_M} = i_S - i_R. \tag{2}$$

The voltage equations on the rotor side are given as follows:

$$0 = -R_R i_R + \frac{d\psi_R}{dt} - j\omega_m \psi_R,\quad \psi_R = \psi_M - L_{\sigma R} i_R. \tag{3}$$

Expanding the value of ψ_R in (3)

$$\frac{d\psi_M}{dt} = R_R i_R + L_{\sigma R}\frac{di_R}{dt} + j\omega_m(\psi_M - L_{\sigma R} i_R). \tag{4}$$

Substituting the value of ψ_M from (3) onto (1)

$$u_S = R_S i_S + R_R i_R + L_{\sigma R}\frac{di_R}{dt} + L_{\sigma S}\frac{di_S}{dt} + \underbrace{j\omega_m \psi_R}_{\approx u_{\text{back EMF}}}. \tag{5}$$

Substituting the value of i_R from (2) onto (5)

$$u_S = R_S i_S + R_R i_R + L_{\sigma R}\frac{di_s - di_\mu}{dt} + L_{\sigma S}\frac{di_S}{dt} + \underbrace{j\omega_m \psi_R}_{\approx u_{\text{back EMF}}}. \tag{6}$$

Due to a high rotor time constant, the main flux linkage can be assumed to be constant $(di_\mu)/(dt) \sim 0$. Substituting in (6)

$$u_S = R_S i_S + R_R i_R + (L_{\sigma R} + L_{\sigma S})\frac{di_s}{dt} + \underbrace{j\omega_m \psi_R}_{\approx u_{\text{back EMF}}} \tag{7}$$

$$\frac{di_s}{dt} = \frac{u_S - R_S i_S - R_R i_R + j\omega_m \psi_R}{L_{\sigma R} + L_{\sigma S}}. \tag{8}$$

The stator voltage is supplied from a standard three-phase inverter, and the inverter can supply six nonzero voltage vectors and two zero vectors. The voltage vector is defined by the switching vector or switching state, and this can be denoted using the gate status of the three bridges of the inverter. The switching state can be written as

$$S_x = [S_a\ S_b\ S_c]$$

where $x \in [0, 1, 2, \ldots, 7]$, and the phase voltages (referred to the star point) can be written as follows (taken from [12]):

$$\begin{bmatrix} u_{an} \\ u_{bn} \\ u_{cn} \end{bmatrix} = \frac{u_{\text{dc}}}{3}\begin{bmatrix} 2 & -1 & -1 \\ -1 & 2 & -1 \\ -1 & -1 & 2 \end{bmatrix}\begin{bmatrix} S_a \\ S_b \\ S_c \end{bmatrix}. \tag{9}$$

Assume a switching state $S_1 = [100]$, and as per (9), the phase voltage can be written as

$$u_{an} = \frac{2u_{\text{dc}}}{3},\quad u_{bn} = -\frac{u_{\text{dc}}}{3},\quad u_{cn} = -\frac{u_{\text{dc}}}{3}$$

$$\begin{bmatrix} u_\alpha \\ u_\beta \end{bmatrix} = \begin{bmatrix} \frac{2}{3} & -\frac{1}{3} & -\frac{1}{3} \\ 0 & -\frac{1}{\sqrt{3}} & -\frac{1}{\sqrt{3}} \end{bmatrix}\begin{bmatrix} u_{an} \\ u_{bn} \\ u_{cn} \end{bmatrix}. \tag{10}$$

Using (10), three-phase voltages are converted to the alpha beta axis, and from there, the stator space vector is calculated

$$u_\alpha = \frac{2u_{\text{dc}}}{3},\quad u_\beta = 0$$

$$u_s = u_\alpha + j u_\beta = \frac{2u_{\text{dc}}}{3}.$$

Applying u_s in (8)

$$\frac{di_s}{dt} = \frac{\frac{2u_{\text{dc}}}{3} - R_S i_S - R_R i_R + j\omega_m \psi_R}{L_{\sigma R} + L_{\sigma S}}. \tag{11}$$

Depending on the selected switching state of the inverter, the stator current can be increased or decreased.

B. Mathematical Analysis—Impact of Stator Currents on the DC-Link Voltage

When the battery is disconnected, the impact of the current i_{pm} (shown in Fig. 1) on the dc-link capacitor is very high since there is no battery. The direction and amplitude of i_{pm} determines the rate at which the dc-link capacitor can charge

or discharge. The dependence of i_{pm} on U_{dc} can be calculated using the expression

$$u_{\text{dc}} = u_{\text{dc}}{}^{\text{init}} + \frac{1}{C}\int i_{\text{pm}} dt. \tag{12}$$

The current i_{pm} is the current coming out of the power module or inverter on the dc side, and this value depends on the switching vector and the position of the current vector at that instant. The current i_{pm} is calculated by applying a dot product of both the switching vector and the current vector

$$i_{\text{pm}} = \begin{bmatrix} S_a & 0 & 0 \\ 0 & S_b & 0 \\ 0 & 0 & S_c \end{bmatrix} \begin{bmatrix} i_a \\ i_b \\ i_c \end{bmatrix} \tag{13}$$

where $[S_a\ S_b\ S_c]$ represents the switching vector and $[i_a\ i_b\ i_c]$ are the phase currents at that particular instant. For example, assume a switching vector SV = [1 0 1], which means that in the first bridge and the third bridge, the top IGBT is turned on, while on the second, the lower IGBT is turned on. Assume an arbitrary stator current vector with phase currents of $I_a = 100$ A, $I_b = -75$ A, and $I_c = -25$ A, and i_{pm} can be calculated as follows:

$$\begin{aligned} i_{\text{pm}} &= i_a * 1 + i_b * 0 + i_c * 1 \\ &= 100 * 1 + -75 * 0 + -25 * 1 = 75 \text{ A} \end{aligned} \tag{14}$$

hence creating a positive value of i_{pm}. Consider another current vector with $I_a = -100$ A, $I_b = 75$ A, and $I_c = 25$, ande i_{pm} can be now calculated as

$$\begin{aligned} i_{\text{pm}} &= i_a * 1 + i_b * 0 + i_c * 1 \\ &= -100 * 1 + 75 * 0 + 25 * 0 = -75 \text{ A}. \end{aligned} \tag{15}$$

By choosing the correct switching vector based on the angle of the current vector, i_{pm} can be chosen to be either positive or negative. These characteristics can be used to manipulate the voltage across the dc-link capacitor.

Two vertically opposite current vectors are chosen, along with six possible nonzero voltage vectors of the inverter. The current i_{pm} is calculated using (13) for each of the current–voltage vector combination, and the evaluated i_{pm} applied on (12) gives the dc-link voltage rise or fall with respect to time (calculated for 10 μs). Figs. 4 and 5 show the effect of different voltage vectors on the dc-link voltage for the two chosen current vectors respectively. All the possible nonzero voltage vectors possible for a three-phase inverter are on the left side, and one of the chosen current vectors in a phasor diagram is also shown. The calculated dc-link voltage change with respect to time for each of the chosen voltage vectors is on the right. Figs. 4 and 5 (on the left) show a hypothetical zero charging line drawn perpendicular to the current vector, and this line cuts the space vector plane into 2 regions. The first region contains the chosen current vector, whereas the second region does not contain the current vector. It can be observed from the right side of the figures that any voltage vector located in region 1 (containing the current vector) discharges the capacitor, while the rest of the voltage vectors lying on region 2 charges the capacitor, any voltage vector exactly on the zero charging line neither charges nor discharges the dc-link capacitor. For example, in Fig. 4, it can

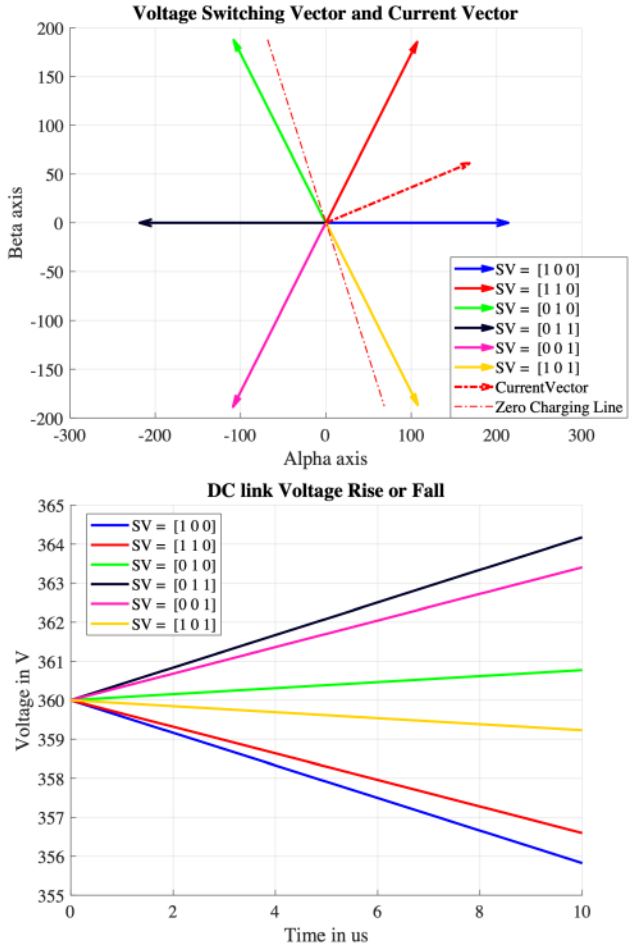

Fig. 4. Impact of current vector on the dc-link voltage. Left: current vector 1 + all possible nonzero voltage vectors. Right: dc-link voltage with respect to time for all possible nonzero voltage vectors applied.

be observed that the voltage vectors SV = [100], [110], [101] discharge the dc-link capacitor, while the remaining voltage vectors charge the capacitor. In Fig. 5, since the chosen current vector is vertically opposite, hence the behavior of the voltage vectors is also vice versa than the first current vector. This is the foundation of the strategy, and based on this theory, further development and analysis of the method are explained.

C. Charging and Discharging Vectors

Fig. 6 shows the equivalent circuit of the three phases of an electric machine with currents flowing at a particular time instant. Here, $L_{\sigma S}$ represents the leakage inductance and u_i represents the back electromotive force (EMF) in the machine. For a given current direction or vector (here, i_a: +ve, i_b: −ve, and i_c: −ve), there are always sets of voltage vectors, which can charge or discharge the capacitor. In Fig. 6, the inductance in the machine acts as a temporary current source, which draws or pumps energy into the capacitor momentarily. The capacitor is connected on the left side of the electric machine, where phase A is connected to $+U_{\text{dc}}/2$, while phases B and C are connected to $-U_{\text{dc}}/2$, and this signifies a voltage vector of [1 0 0]. The capacitor on the right side of the electric machine, where phase A is connected to $-U$dc/2, while phases B and C are connected to $+U_{\text{dc}}/2$, and this signifies a voltage vector

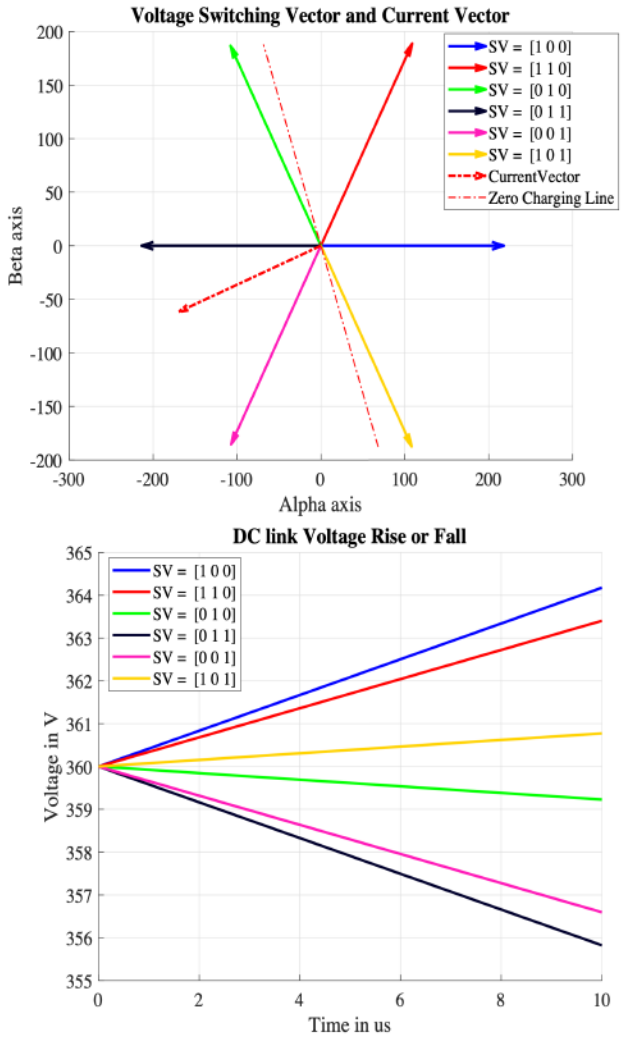

Fig. 5. Impact of current vector on the dc-link voltage. Left: current vector 2 + all possible nonzero voltage vectors. Right: dc-link voltage with respect to time for all possible nonzero voltage vectors applied.

of [0 1 1]. The voltage vector configuration on the right side would charge the dc-link capacitor, whereas the configuration on the left side would discharge the dc-link capacitor. Since the inductance of the phase windings resists any change in the currents, $L(di/di)$ forces the currents to flow toward or away from the capacitor and also charge or discharge the capacitor. The currents in the electric machine would behave inversely to the dc-link voltage, which means that discharging the capacitor would mean an increase in the stator currents and also vice versa. The exchange of energies between the electric machine and the dc-link capacitor can be described by the energy equation

$$\Delta E_{\text{cap}} = \Delta E_{\text{induLeak}} + E_{\text{shaft}} - E_{\text{res}}. \tag{16}$$

1) E_{cap} : Energy stored in the capacitor.
2) E_{induLeak} : Energy stored in the leakage inductance.
3) E_{shaft} : Energy received or send depending on whether it is (mot\gen).
4) E_{res} : Energy dissipated as ohmic losses in the machine.

Using a three-phase inverter shown in Fig. 1, eight different voltage vectors can be applied to the machine. For each angle

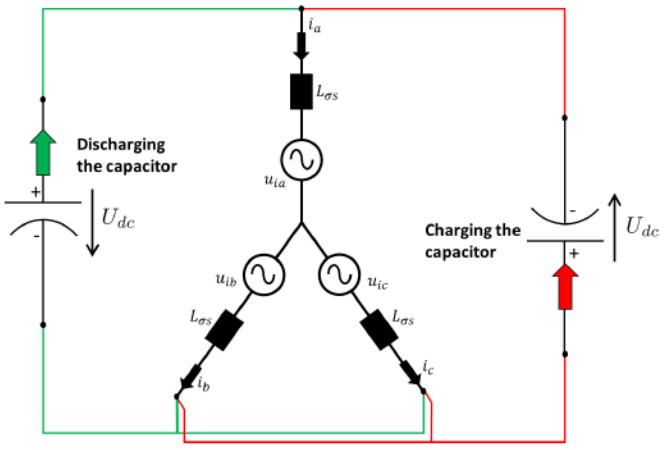

Fig. 6. Charging and discharging the capacitor.

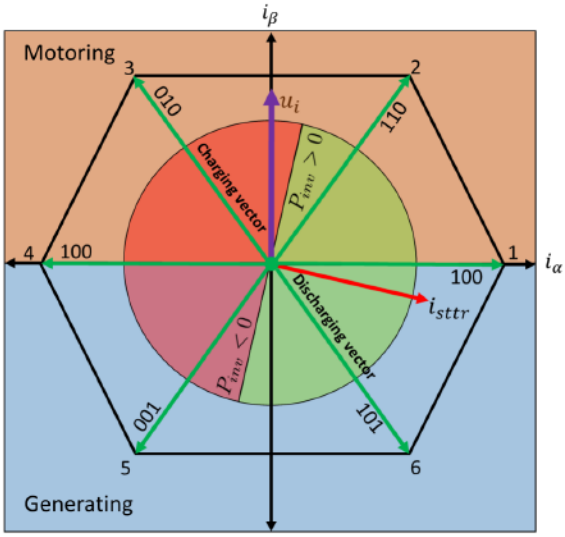

Fig. 7. Charging and discharging vectors.

of the stator current (i_{sttr}), a voltage vector either with a positive or negative Δegy_{cap} can be chosen, which then would charge or discharge the dc-link capacitor.

D. Charging and Discharging Vectors on the Phasor Diagram

Fig. 7 shows the current vector i_{sttr} and the back EMF u_i of an induction machine in the phasor diagram at the moment when the machine is operating in the generating mode. The six possible nonzero voltage vectors (1–6) in the α–β axis are also shown. The space vector area has been classified depending upon two different criteria.

1) *Operating Point of the Machine (Motoring\Generating):* At this particular instant, the back EMF of the machine u_i lies at the β-axis, making the α–β axis coincide with the d–q axis. Therefore, the first and second quadrants (rectangular brown area) represent the motoring region and the third and fourth quadrants (rectangular blue area) represent the generating region.
2) *Charging and Discharging Region:* The area can also be classified into regions where the instantaneous power output from the inverter (17) is either positive or negative depending on the position of the current vector.

The green semicircular region in Fig. 7 has a positive power output of the inverter, whereas the red semicircular region has a negative power output. A positive power output means that the inverter is drawing energy from the dc side, that is, the energy flow is from the dc-link capacitor to the machine side, and vice versa for negative power. Hence, any voltage vector selected on the positive power output region will discharge the capacitor, while the vectors selected on the red semicircular region will charge the capacitor

$$P_{\text{inv}} = u_s.i_s. \tag{17}$$

The uncontrolled rise of dc-link voltage during generating can be stopped by applying alternating discharging and charging vectors. Alternating DV and CV voltage vectors would make sure that both the dc-link voltage and stator currents are in the safe limits. The charging vector is chosen from the red semicircular region, while the discharging vector is chosen from the green semicircular region. Simulations showed that a stable combination of charging and discharging vector is voltage vectors 3 and 6, with respect to the current vector i_{sttr}, as shown in Fig. 7. All the other voltage vectors combination would change the amplitude and angle of the current vector very fast and it becomes more difficult to contain the current amplitude inside the band where it is safe for the device to operate. More details about the simulations are in Section IV-C. The thumb rule used in this article to identify the discharging vector is to find the voltage vector leading the current in the same sector, and the charging vector would be vertically opposite to the discharging vector. Applying these vectors sequentially for a finite number of steps will make the current vector rotate in the vector plane. This behavior will cause the machine to oscillate between the motoring and generating region, hence dissipating the energy as mechanical output in the shaft and resistive losses in the phase windings. This strategy is termed as safe turn-off (STO) in this article.

IV. Implementation

The strategy is tested on an induction motor drive for an electric vehicle. The electric drive unit consists of the housing with the three-phase inverter and the main microcontroller responsible for the functions of the electric drive, such as torque control. The drive unit also has a CPLD chip, which is a smaller controller with limited memory. The CPLD has a faster clock frequency than the main controller, which makes it quicker to respond. Most of the fault detection checks and the fault reactions are programmed in the CPLD, and they talk directly to the gate driver of the power module. A fast reaction from the hardware is required when the electric drive system is in a state of uncontrolled generation so that the dc-link capacitor and the power module are not damaged. Hence, the strategy was programmed on a CPLD, which reacts faster than the main microcontroller.

A. Current Vector Identification

For the proposed STO to work, it is essential that the position of the current vector is calculated correctly. The vector identification must be simple and robust. The method described here compares the instantaneous values of currents in three of the phases and estimates the current vector location inside a sector. Three comparators were used, as shown in Fig. 8. The inputs to each of the comparators are connected to consecutive current sensors and give the signals shown in the following equation:

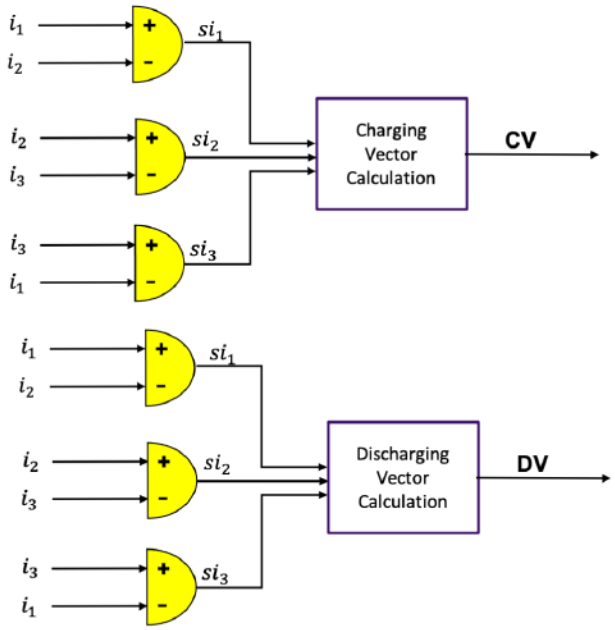

Fig. 8. Current vector identification.

$$\text{si}_1 = (\text{i}_1 > \text{i}_2) \tag{18a}$$

$$\text{si}_2 = (\text{i}_2 > \text{i}_3) \tag{18b}$$

$$\text{si}_3 = (\text{i}_3 > \text{i}_1) \tag{18c}$$

$$\text{si} = [\text{si}_1 \ \ \text{si}_2 \ \ \text{si}_3] \tag{18d}$$

where si_1, si_2, and si_3 denote the output of the comparators shown in Fig. 8. i_1, i_2, and i_3 denote the instantaneous value of stator currents measured using current sensors. The expression *si* in (18d) gives the location information of the current sector on the space vector plane. Consider Fig. 9, if $si = [1\ 0\ 0]$, and then, the location of the current vector will be in the sector highlighted red in the figure. Using this information, an approximate position of the current vector can be calculated and hence calculate the correct charging and discharging vectors.

B. Fault Reaction Algorithm

A voltage-divider circuit combined with a comparator is used to create an overvoltage detection mechanism, and this creates an overvoltage flag for the dc-link voltage. Whenever the dc-link voltage is above the threshold, a flag is sent to the CPLD to commence the start of the strategy. The overvoltage flag along with the output from the current comparators to estimate the current vector location serves as an input to the CPLD. The discharging and charging vectors are then calculated from the current vector location. As described in Section III-C, the discharging vector is the voltage vector leading the current in the same sector, and the charging vector would be vertically opposite to the discharging vector. The

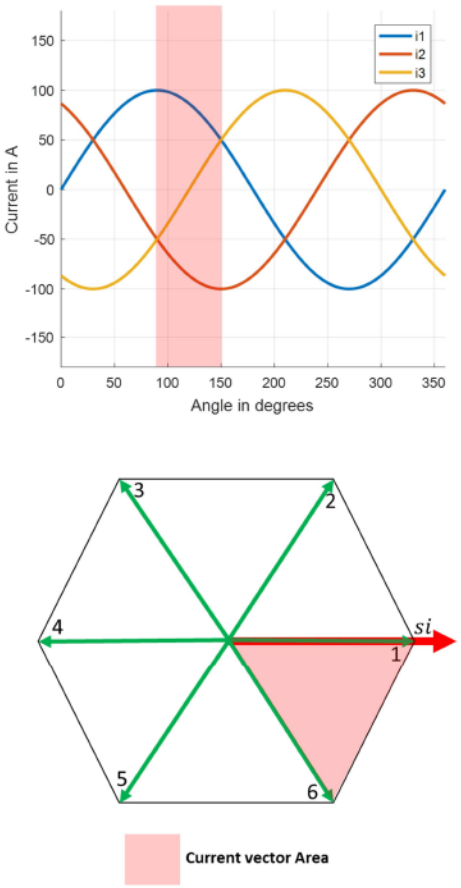

Fig. 9. Current sector identification.

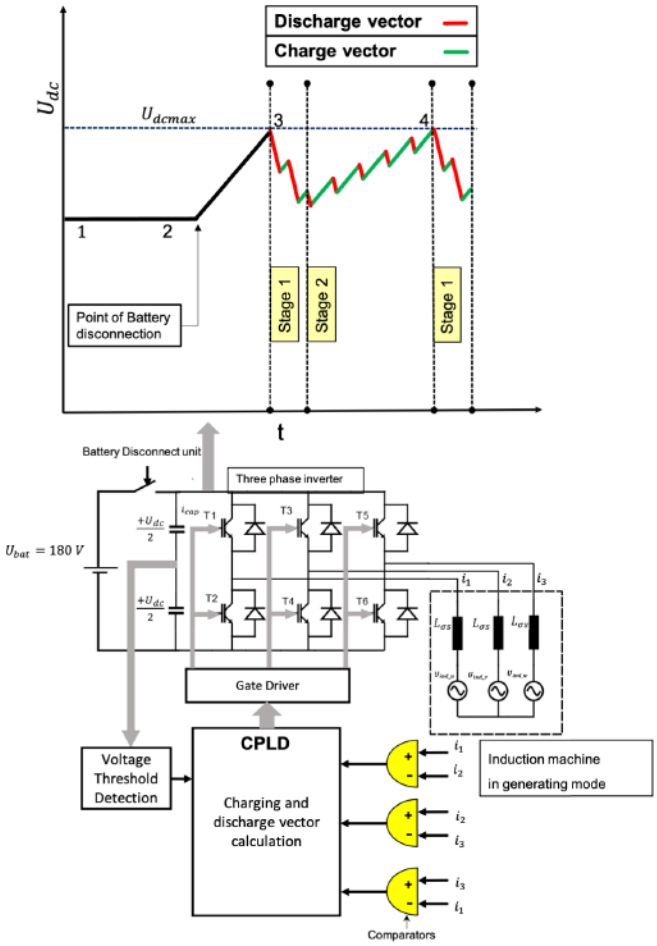

Fig. 10. STO during battery disconnection: proposed algorithm.

identified vectors are then applied sequentially for a finite number of pulsewidth modulation (PWM) periods. A PWM period consists of a discharging period and a charging period, and a ratio DV:CV is calculated, which determines whether the overall voltage gradient is positive or negative in the dc-link capacitor. When switching frequency in the inverter is 10 kHz, the length of one time period is 100 μs. If the ratio DV:CV is 80:20, first, 80-μs discharging voltage vector is applied, and last, 20-μs charging vector is applied. Using this ratio as a control parameter and the feedback from the overvoltage flag, the dc-link voltage is controlled to a constant value.

The STO strategy is split into two stages. In the first and stages, the ratio DV:CV is chosen so that the dc-link voltage gradient is negative and positive, respectively. When the controller receives an overvoltage flag, stage 1 is initiated for a finite number of PWM periods ($n1$). During stage 1, the dc-link voltage decreases to a value smaller than the voltage threshold. After $n1$ number of PWM periods, stage 2 is initiated and continued until there is an overvoltage flag or $n2$ number of PWM periods. Due to a positive voltage gradient, the dc-link voltage would increase back to the value of the threshold. This discharging and charging behavior of the strategy will maintain the voltage under the voltage limit, as shown in Fig. 10. In this figure, in stage 1, the DV:CV ratio was set to 80:20, and later in stage 2, the DV:CV ratio was set back to 20:80. A state machine diagram is shown in Fig. 11, which explains the conditions on which the transitions between

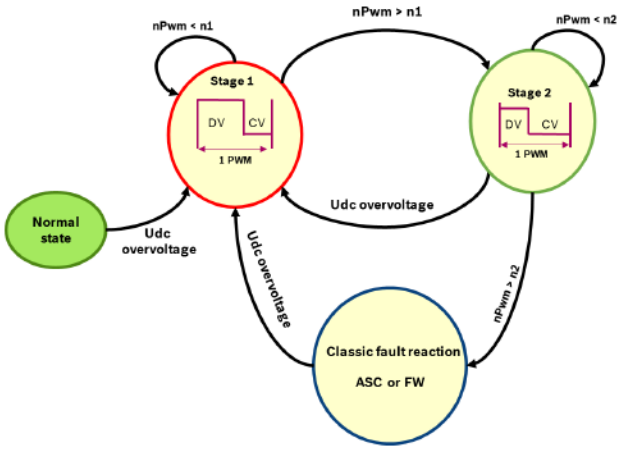

Fig. 11. State flow: STO.

stages 1 and 2 and finally to the classic safe states are performed. The proposed strategy acts like an intermediate step that helps to avoid any overcurrents or overvoltages, which happens when directly going to any of the classic safe states. If there was a dc-link voltage sensor, instead of the comparator with voltage-divider circuit, the dc-link voltage could be controlled with more accuracy. The idea of the two stages is to save the cost of such a sensor, which should also be reliable when the fault happens.

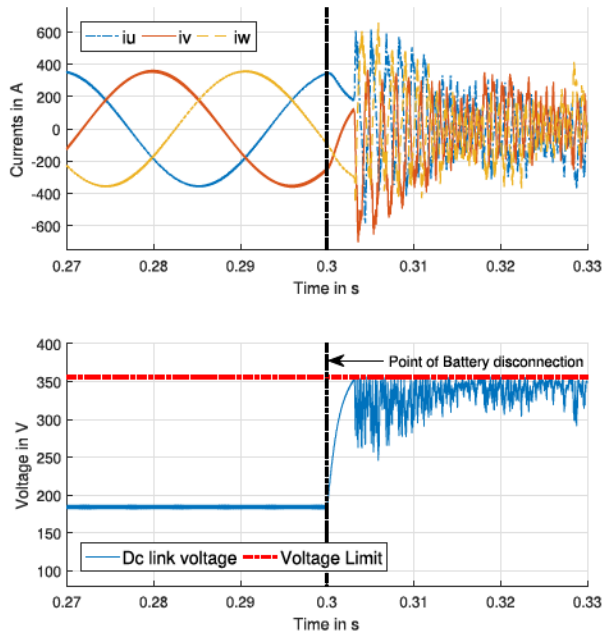

Fig. 12. Simulation at 1000 r/min and −100 Nm.

TABLE I
OPTIMIZED PARAMETERS FOR STO

Stage1	Stage2
DV:CV 80:20	DV:CV 20:80
n1=2	n2=20

C. Simulation Results

STO was simulated in a MATLAB/Simulink model for a 90-kW induction machine drive over the entire torque–speed map. The simulation model consists of a dq model of the induction machine, a three-phase Inverter source, and a controller. The STO algorithm is programmed in the inverter module, which activates when there is an overvoltage fault. Using the model, the DV:CV ratio and $n1$ were varied and optimized for minimum stator current and dc-link overvoltage using iterative simulations. One of the best combinations of possible DV:CV ratio and $n1$ is given in Table I. Fig. 12 shows the output from the simulation at 1000 r/min and −100 Nm using the chosen ratio. In Fig. 12, the battery was disconnected at $t = 0.3$, and the dc-link voltage increases because of the uncontrolled generating mode. The STO strategy commences when the dc-link voltage reaches the threshold of 355 V. The dc-link voltage charges and discharges after every PWM cycle, maintaining the voltage under the threshold as expected.

V. LOSS MODELING

The simulations in Section IV-C are done using a dq fundamental model of the induction machine, which does not consider any high-frequency losses in the machine, and also, the inverter losses in the model were also ignored. The dc-link voltage calculation in the simulation model is done using the current i_{pm} going into the inverter as described in [4]. The current i_{pm} should reflect all the losses in the electric drive system so that the dc-link voltage is calculated accurately. In this section, two major losses are going to be considered so that the described simulation model is closer to reality.

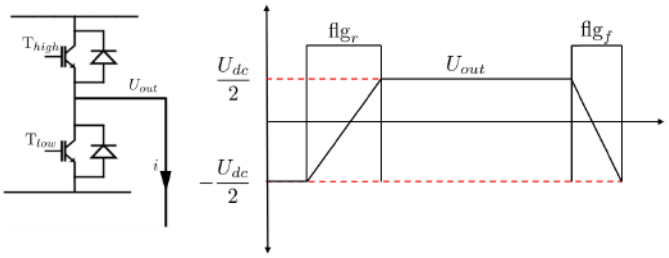

Fig. 13. Definition of flg_r and flg_f.

1) *Inverter Losses:* Conduction losses + switching losses.
2) High-frequency conduction losses in the rotor bars of the induction machine.

A. Inverter Losses

Not all the dc power entering the inverter ends up on the other ac side, there are losses dissipating in the IGBTs as both conduction and switching losses. These losses must be calculated and included in the simulation so that the input dc power is calculated correctly and hence also the voltage across the capacitor. In this analysis, the losses occurring across the capacitor are neglected.

1) Conduction Loss: Depending on the direction of the current flow and the voltage vector applied, it can be determined if the current flows through the diode or the IGBT. With this information, the conduction losses of each bridge can be calculated as in the following equation:

$$P_{\text{cond}} = \begin{cases} U_{\text{ce}} i, & \text{if current flows through IGBT} \\ U_{\text{fw}} i, & \text{if current flows through diode.} \end{cases} \tag{19}$$

Both U_{ce} (collector–emitter voltage of the IGBT) and U_{fw} (forward voltage of the diode) are obtained from the data sheet of the switching device.

2) Switching Loss: The data sheet of the IGBT power module provides the following information about its switching characteristic.

1) Eon_{igbt} *and* $Eoff_{igbt}$: Energy consumed during turn-on and turn-off for the IGBT.
2) $\text{Eoff}_{\text{diode}}$: Energy consumed during turn-off of the diode.

Fig. 13 defines two flags flg_r and flg_f that are set when the voltage output (U_{out}) of the bridge is either rising or falling, respectively, and these variables are updated throughout the simulation process and are used to calculate the switching losses. Table II explains which device is conducting during either a voltage rise or voltage fall in a single bridge of the inverter. Based on these conditions and using the information from the data sheet, the expression to calculate the switching losses has been summed up in the following equation:

$$P_{\text{switch}} = \frac{\text{Eon}_{\text{igbt}}}{t_{\text{on}}} \text{flg}_r + \frac{\text{Eoff}_{\text{diode}}}{t_{\text{off}}} \text{flg}_r + \frac{\text{Eoff}_{\text{igbt}}}{t_{\text{off}}} \text{flg}_f, \quad \text{if } i \geq 0 \tag{20a}$$

$$P_{\text{switch}} = \frac{\text{Eoff}_{\text{igbt}}}{t_{\text{off}}} .\text{flg}_r + \frac{\text{Eoff}_{\text{diode}}}{t_{\text{off}}} \text{flg}_f + \frac{\text{Eon}_{\text{igbt}}}{t_{\text{on}}} \text{flg}_f, \quad \text{if } i < 0. \tag{20b}$$

After calculating the conduction and switching losses, the new i_{pm} is calculated as in (21). i_{pm} now includes the

TABLE II
CONDUCTION STATES OF IGBT AND DIODE DURING SWITCHING

	$i \geq 0$	$i < 0$
U_{out} rising	High side IGBT turned on Low side diode turned off	Low side IGBT turned off High side diode turned on
U_{out} falling	High side IGBT turned off Low side diode turned on	Low side IGBT turned on High side diode turned on

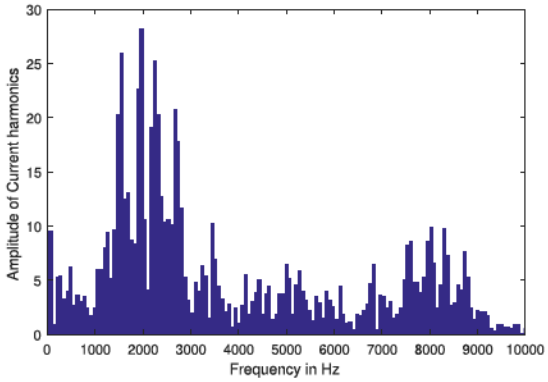

Fig. 14. FFT of the stator current during STO.

effect of the inverter losses and is now used to calculate the new dc-link voltage

$$i_{\text{pm}_{\text{new}}} = \frac{u_{\text{dc}} i_{\text{pm}_{\text{old}}} - (P_{\text{cond}} + P_{\text{switch}})}{U_{\text{dc}}}. \tag{21}$$

B. High-Frequency Losses in the Rotor

Fig. 14 shows the fast Fourier transform (FFT) of the stator currents during STO. During STO, the currents are no longer normal sinusoidal signals; instead, they consist of higher order harmonics (1 kHz and above) that are well beyond the fundamental frequency of the stator currents. This creates high-frequency losses in the machine, which are mainly high copper losses in the rotor due to deep bar effects or skin effect in the rotor slots. Due to the higher current harmonics seen in Fig. 14, it can be assumed that the stator flux directly interacts with the rotor bar with a slip equal to 1, and this will induce high-frequency currents in the rotor bars. These high-frequency currents in the rotor bar will force the current to flow only through a small portion of the bar (skin effect), and this increases the effective resistance of the rotor bar and also the losses. This frequency-dependent characteristics of the rotor resistance needs to be incorporated into the simulation model so that the high-frequency conduction losses can be accurately estimated

$$\delta = \sqrt{\frac{\rho}{\pi f \mu_0}}. \tag{22}$$

Equation (22) calculates the depth where the current will flow depending on the frequency of the applied currents on the rotor bars. In [14], a parameter $\xi = h/\delta$ is defined, where h is the height of the rotor bar and δ is the skin depth. This factor is used to calculate the frequency dependence of the rotor resistance and rotor inductance which is multiplied and is shown in the following equation:

$$K_r = \xi \frac{\sinh(2\xi) + \sin(2\xi)}{\cosh(2\xi) - \cos(2\xi)} \tag{23a}$$

$$K_x = \xi \frac{\sinh(2\xi) - \sin(2\xi)}{\cosh(2\xi) - \cos(2\xi)}. \tag{23b}$$

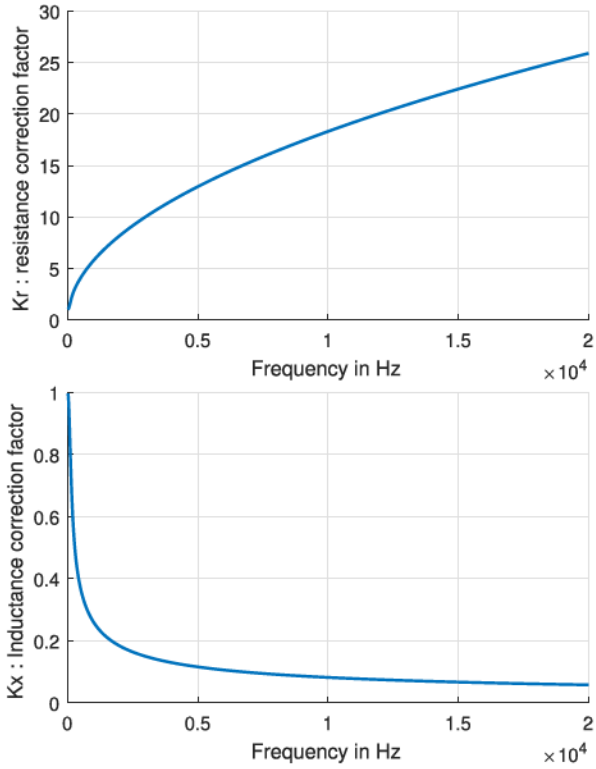

Fig. 15. Rotor bar resistance and reactance correction factors.

In (23), both K_r and K_x are the correction factors depending on the frequency that is multiplied with the dc values of R_r and L_r. Fig. 15 shows the increase in rotor bar resistance and the decrease in the rotor leakage inductance with frequency. This change in the parameter needs to be incorporated into the dq model in time domain so that the high-frequency losses are correctly calculated. Equation (24) shows the frequency-dependent resistance and inductance derived from the dc values using the correction factors

$$R_{\text{ac}} = K_r R_{\text{dc}} \tag{24a}$$

$$L_{\text{ac}} = K_x L_{\text{dc}}. \tag{24b}$$

C. RL-Ladder Circuit

The next step is to achieve a frequency-dependent rotor resistance time-domain model, which is simple enough to yield reasonable simulation times. The impedance–frequency characteristics of rotor conductor can be modeled using simple networks of resistances and inductances as explained in [17]. Several publications use this method to simulate the dynamic model of induction machine with skin effect [15], [16], [18]. In this article, the frequency-dependent resistance is modeled by using an RL-ladder circuit as illustrated in the dissertation in [13]. The rotor bar can be assumed to be divided into different sections, as shown in Fig. 16, and each section can be represented as a resistance along with a leakage inductance in the RL-ladder circuit. This allows to have nonuniform current density in a single rotor bar. Since the current density is higher at the top of the bar, it makes more sense that the height of the section is the smallest at the top of the rotor bar and slowly

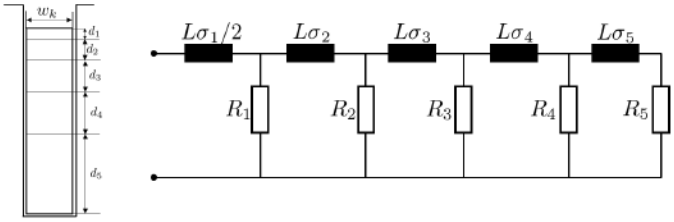

Fig. 16. RL-ladder circuit for the rotor bar.

increasing to the bottom. Fig. 16 shows the RL-ladder circuit which replaces R_r (rotor resistance) in the dq equivalent circuit used in the simulation model. This RL-ladder circuit makes the lower frequency components to flow through the farthest resistance, while the high-frequency components will flow through the nearer resistances. The values of resistances and inductances in the ladder circuit must be tuned to match the real frequency-dependent rotor bar resistance. The total resistance and reactance of the ladder circuit is calculated by representing the circuit using state space equations. Followed by this, the RL-ladder circuit is transformed into the Laplace domain, through which the frequency-dependent resistance and reactance of the circuit can be calculated. The step-by-step procedure is explained in [13] and will not be explained further in this article. The final model impedance of the ladder circuit can be written as in the following equation:

$$\dot{X} = AX + BU \tag{25a}$$

$$y = CX + DU \tag{25b}$$

$$Z(s) = \frac{1}{C(\mathrm{SI} - A)^{-1}B + D}. \tag{25c}$$

With $S = 2\pi f$

$$Z(j\omega) = R_l + jX_l \tag{26}$$

where R_l and X_l are the frequency-dependent total resistance and reactance of the ladder circuit, respectively. Each RL group in the ladder circuit (Fig. 16: R_i and L_i) can be represented as a section in the rotor bar with its own resistance and inductance written as in the following equation:

$$R_i = \frac{\rho l}{d_i w_k} \tag{27a}$$

$$L_i = \frac{\mu_0 l d_i}{w_k} \tag{27b}$$

$$\sum_{i=1}^{5} d_i = h. \tag{28}$$

In (27c), w_k denotes the width of the slot and d_i represents the height of the ith section of the rotor bar. This resistance and inductance represent one RL group in the ladder network. A total of five layer or RL group ladder networks is considered in the model to include the skin effect losses. A parameter search is performed on the RL ladder network by keeping the frequency-dependent characteristics of R_{ac} and L_{ac} from (24) as a reference. The optimum parameters for the ladder circuit are searched, which holds the criteria in (27c), and these criteria makes sure that the total height of the rotor bar remains constant. An optimization run in MATLAB is performed

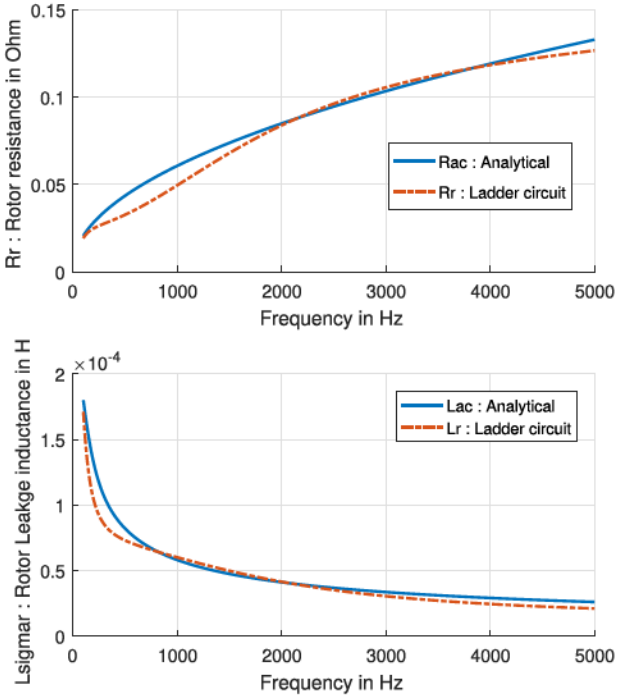

Fig. 17. Optimization of the RL ladder parameters to fit the analytical expression.

using fminsearch, which minimizes the normalized objective function mentioned in the following equation:

$$\varepsilon_r = \left(\frac{R_{ac} - R_l}{R_{ac}}\right)^2 \tag{29a}$$

$$\varepsilon_l = \left(\frac{L_{ac} - L_l}{L_{ac}}\right)^2. \tag{29b}$$

Fig. 17 shows the result from the optimization algorithm, and the RL-ladder circuit has the expected frequency-dependent resistance characteristics. This optimized RL-ladder circuit is replaced in the dq circuit for rotor resistance R_r of the induction machine. This new model would be used to compare with the measurements done in Section VI.

VI. Measurements and Analysis

A. Measurement Setup

The measurement setup consists of a 90-kW induction machine coupled to a load machine, the inverter unit, battery emulator, and a mechanical disconnect unit between the battery and the inverter unit. The inverter unit consists of the power module, gate drive circuits, microcontroller unit, dc-link capacitor, and also the busbars on both the ac and dc sides. The specification of the measurement setup is shown in Table III. The measurement setup is shown in Fig. 18, and the inverter casing is open to tap out gate signals to the inverter. The microcontroller unit is responsible for the main functionality of the system like torque control of the system. The STO strategy has been programmed in a CPLD, which is a programmable logic device and can function immediately on startup. All the commands that are time-critical are done here. Three comparators to determine the phase current sector have

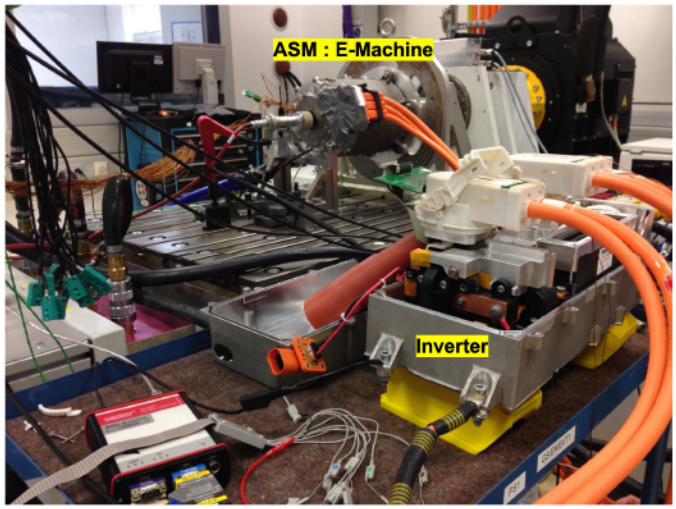

Fig. 18. Measurement setup.

TABLE III
SPECIFICATION OF THE MEASUREMENT SYSTEM

Nominal DC-link Voltage	350V
Nominal Phase Current	380 A (rms)
Rated Power	90 kW
Switching Frequency	10 kHz
Modulation technique	SVPWM
Coolant Flow	10 lpm

been added to the inverter unit and this output was connected to the CPLD. The output from the CPLD interacts directly with the gate driver of the IGBT of the inverter. The dc-link voltage was set to 180 V and the voltage threshold for the commencement of the strategy was set to 356 V, and this provides a buffer for the inverter to operate under a safe operating voltage. The PWM duty cycle during STO has been chosen with a DV/CV ratio of 20/80 (positive gradient) in stage 1 with $n1 = 6$ and a DV/CV ratio of 30/70 in stage 2 (positive gradient). The ratio is chosen so that the capacitor does more charging than discharging, and hence, an overall positive gradient of voltage is expected. The dc voltage was provided by a battery emulator, which provides the voltage for the system. A mechanical switch was connected in between the battery and dc-link capacitor, which is used as the disconnect unit. Measurements were done for different operating points and the results were compared with simulation results.

B. Analysis and Discussion

Fig. 19 shows the comparison between measurement and the simulation of the operating point at 1000 r/min and -100 Nm with no loss model (skin effect in the rotor bar + inverter losses excluded). At $t = 0.28$, the battery is disconnected, creating a condition of uncontrolled generation in the dc-link capacitor. In the simulation model, the dc-link voltage is rising up after it reaches the threshold of 356 V because of a chosen positive gradient ratio selection for DV:CV, whereas the dc-link voltage in the measurement is falling down after the voltage reaches the threshold. In Fig. 20, the same comparison is made with the measurements, but now, the simulation model with the extra losses (extra copper loss due to skin effect + Inverter losses) is used. The comparison in Fig. 20 shows

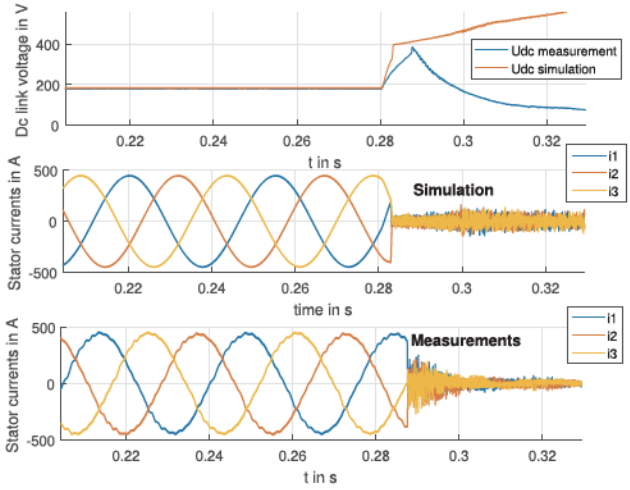

Fig. 19. Comparison of the simulation model (no-loss model included) and measurements at 1000 r/min and 100 Nm.

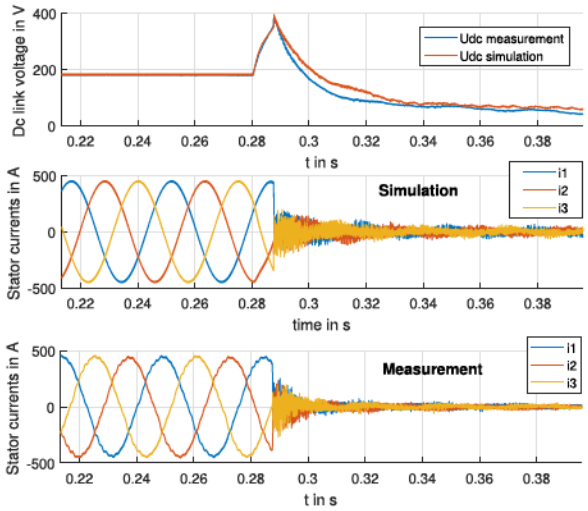

Fig. 20. Comparison of the loss inclusive simulation model and measurement at 1000 r/min and 100 Nm.

that the simulation and measurement match very well and proves that the calculation of the extra losses in the inverter and the high-frequency losses in the rotor bar is vital for accurate simulation of the dc-link voltage. The characteristic exponentially decaying dc-link voltage in the simulation proves that skin effect is one of the major reasons behind this behavior. Higher frequency of stator current increases the high-frequency losses in the induction machine, and hence, the skin effect acts like a positive reinforcement for the STO strategy. The important takeaway from the above comparison is that the energy exchange between the dc-link capacitor and the inductance of the machine is comparatively less than the energy dissipated in the rotor windings of the induction machine. This is the reason why a positive gradient DV:CV ratio still creates a drop in the dc-link voltage. Fig. 21 shows the torque characteristics during STO at 1000 r/min and -100 Nm and no unwanted or dangerous torques are produced at this operating point. Fig. 22 shows the comparison between results from the loss inclusive simulation model and measurements at 3000 r/min and -100 Nm. The STO strategy has been successfully validated using measurements. Experimental comparison with ASC measurements for the

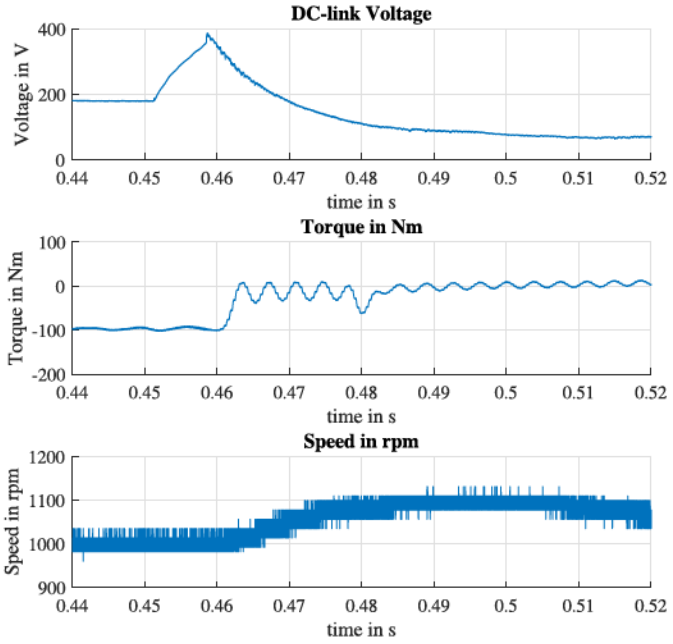

Fig. 21. Measurements—torque and speed values during STO at 1000 r/min and −100 Nm.

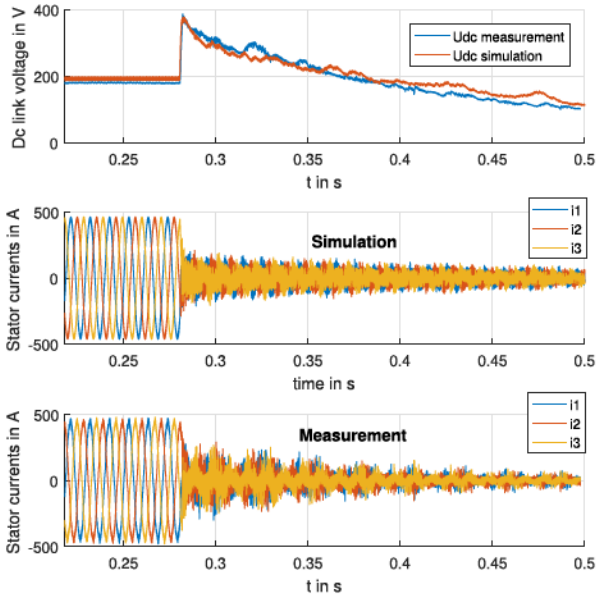

Fig. 22. Comparison of the loss inclusive simulation model and measurement at 3000 r/min and −100 Nm.

same operating points was not carried out, as the currents are too high (simulated in Section II-A: 1390 A) and it could potentially damage the inverter. The peak currents at the same operating point in the measurement for STO strategy are way smaller than shown in measurements in both the operating points. Measurements for FW are also done in [4] with the induction machine; in FW, a dc-link transient voltage peak is inevitable and always higher than the dc-link voltage during STO. Results in Table IV show the comparison between the turn-off strategies **ASC**, **FW**, and the proposed STO strategy at 1000 r/min and −100 Nm. With the proposed strategy, the post-fault currents are smaller than the ASC current of 1380 A, and also, the dc-link voltage always stays inside the threshold of 356 V, which is smaller than the dc-link voltage

TABLE IV
CLASSIC TURN-OFF VERSUS STO

ASC (Simulations)	**FW** (Simulations)	**STO** (Measurements)
Peak i_{sttr}= 1390 A	Δu_{dc}= 30 V	Peak i_{sttr}= 603 A Δu_{dc}= 0 V
No transient DC-link voltage Peaks, but high stator current overshoots	Transient DC-link voltage Peaks with no stator current overshoots	No stator current overshoots and transient DC-link voltage Peaks
Higher currents overshoots leads to torque overshoots	No current overshoots and hence no torque overshoots	Small ringing effect in the torque as seen in Fig. 21
Can be implemented in a CPLD without any current vector location	Can be implemented in a CPLD without any current vector location	Can be implemented in a CPLD with current location information using comparators

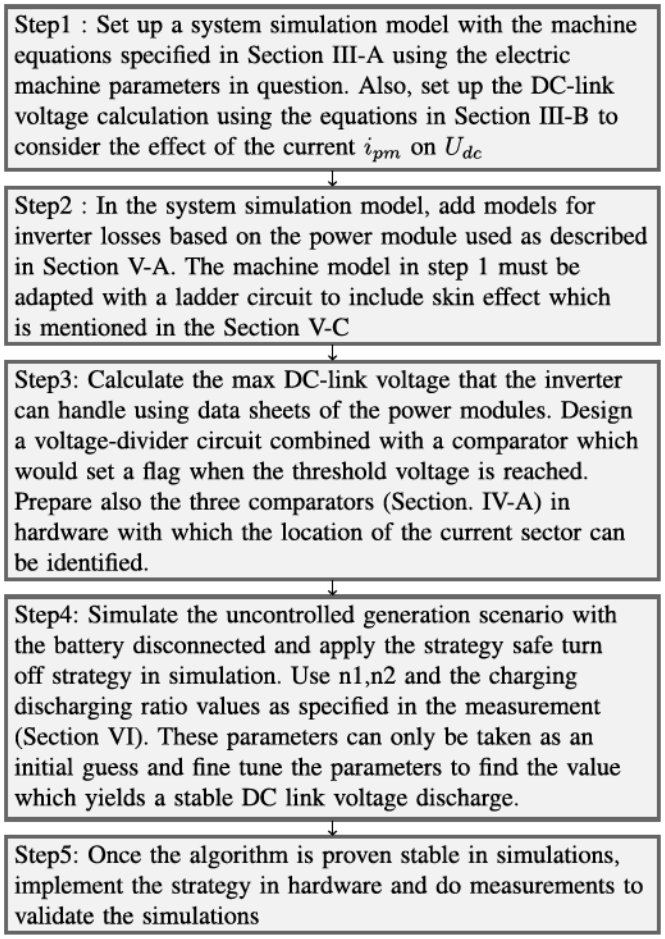

Fig. 23. STO—workflow.

peak in FW. Fig. 23 shows the various steps that were followed in this publication to develop the strategy. This workflow will evolve once different power class machines and inverter are analyzed and setup as part of future works

VII. CONCLUSION

A method to safely turn-off an electric drive without a transient peak in the dc-link capacitor and low stator currents has been proposed. In this method, the energy between the inductance of the machine and the dc-link capacitor is transferred by applying charging and discharging voltage vectors

based on the location of the current vector. During the strategy, the frequency of the stator currents was observed to be very high compared to the fundamental, and this increases the skin effect in the rotor bars of the machine and correspondingly more resistance in the rotor bar. This higher rotor resistance increases the energy dissipation and hence quickly discharging the dc-link capacitor faster. The strategy was tested using a simulation model in MATLAB/Simulink. The major losses, such as the inverter losses and the rotor ohmic losses, were incorporated into the simulation model. The algorithm was realized in a CPLD, which can directly control the gate driver of the IGBTs in a standard three-phase inverter and the measurements were done with an induction machine drive. The results showed no transient peak in the dc-link capacitor and less stator currents, hence validating the strategy. Using this turn-off method in an electric drive system causes less stress on the dc-link capacitor, IGBTs, and the electric machine, hence requiring a smaller dc-link capacitor, IGBTs with lower voltage rating, and electric machine with lower current rating and thereby reducing the cost of the overall system.

REFERENCES

[1] B. A. Welchko, T. M. Jahns, W. L. Soong, and J. M. Nagashima, "IPM synchronous machine drive response to symmetrical and asymmetrical short circuit faults," *IEEE Trans. Energy Convers.*, vol. 18, no. 2, pp. 291–298, Jun. 2003.

[2] T. M. Jahns and V. Caliskan, "Uncontrolled generator operation of interior PM synchronous machines following high-speed inverter shutdown," *IEEE Trans. Ind. Appl.*, vol. 35, no. 6, pp. 1347–1357, Nov./Dec. 1999.

[3] C. Z. Liaw, W. L. Soong, B. A. Welchko, and N. Ertugrul, "Uncontrolled generation in interior permanent-magnet machines," *IEEE Trans. Ind. Appl.*, vol. 41, no. 4, pp. 945–954, Jul./Aug. 2005.

[4] A. R. Chandran, M. Hennen, and A. Arkkio, "Analytical investigation of DC link overvoltages during freewheeling for inverters in EV," in *Proc. IEEE Transp. Electrific. Conf. Expo (ITEC)*, Dearborn, MI, USA, Jun. 2016, pp. 1–6.

[5] B. A. Welchko, T. M. Jahns, and S. Hiti, "IPM synchronous machine drive response to a single-phase open circuit fault," in *Proc. 16th Annu. IEEE Appl. Power Electron. Conf. Expo. (APEC)*, Anaheim, CA, USA, 2001, pp. 421–427.

[6] K. Lu, Y. Zhu, Z. Wu, and M. Xiao, "Suppression of current fluctuations and the brake torque for PMSM shutoff in electric vehicles," *Math. Problems Eng.*, vol. 2019, pp. 1–13, Sep. 2019, doi: 10.1155/2019/5026316.

[7] M. Merkel, T. Merkel, G. Plapp, A. König, and L. Xie, "Vorrichtung und verfahren zum betreiben einer elektrischen maschine," Deutsches Patent 10 201 226 564.6, Jun. 25, 2015.

[8] Z. Ke, J. Zhang, and M. W. Degner, "DC bus capacitor discharge of permanent magnet synchronous machine drive systems for hybrid electric vehicles," in *Proc. IEEE Appl. Power Electron. Conf. Expo. (APEC)*, Long Beach, CA, USA, Mar. 2016, pp. 241–246, doi: 10.1109/APEC.2016.7467879.

[9] J.-I. Itoh, W. Aoki, G. T. Chiang, and A. Toba, "Suppression method of rising DC voltage for the halt sequence of an inverter in the motor regeneration," in *Proc. IEEE Energy Convers. Congr. Expo.*, Denver, CO, USA, Sep. 2013, pp. 188–195.

[10] J. I. Itoh, W. Aoki, G. T. Chiang, and A. Toba, "Uniform provisions concerning the approval of vehicles with regard to the protection of the occupants in the event of a frontal collision," United Nation Econ. Commission Europe Vehicle Regulation, Geneva, Switzerland, Tech. Rep. No.94 (ECE R94), Aug. 2013.

[11] R. W. De Doncker, D. W. J. Pulle, and A. Veltman, *Advanced Electrical Drives*. London, U.K.: Springer, 2011.

[12] S. N. Manias, *Power Electronics and Motor Drive Systems*. New York, NY, USA: Academic, 2017, pp. 271–500, doi: 10.1016/B978-0-12-811798-9.00006-8.

[13] O. I. Okoro, "Dynamic and thermal modelling of induction machine with non-Linear effects," M.S. thesis, Dept. Elect. Mach., Kassel Univ., Kassel, Germany, 2002.

[14] P. L. Alger, *The Nature of Induction Machines*. London, U.K.: Gordon and Breach, 1965.

[15] E. A. Klingshirn and H. E. Jordan, "Simulation of polyphase induction machines with deep rotor bars," *IEEE Trans. Power App. Syst.*, vol. PAS-89, no. 6, pp. 1038–1043, Jul. 1970.

[16] D. Lin and P. Zhou, "An improved dynamic model for the simulation of three-phase induction motors with deep rotor bars," in *Proc. Int. Conf. Electr. Mach. Syst.*, Wuhan, China, Oct. 2008, pp. 3810–3814.

[17] D. S. Babb and J. E. Williams, "Network analysis of A-C machine conductors," *Trans. Amer. Inst. Electr. Eng.*, vol. 70, no. 2, pp. 2001–2005, Jul. 1951, doi: 10.1109/T-AIEE.1951.5060665.

[18] W. Levy, C. F. Landy, and M. D. McCulloch, "Improved models for the simulation of deep bar induction motors," *IEEE Trans. Energy Convers.*, vol. 5, no. 2, pp. 393–400, Jun. 1990, doi: 10.1109/60.107238.

Aravind Ramesh Chandran was born in Trivandrum, India, in 1989. He received the M.Sc. (Tech.) degree from Aalto University, Espoo, Finland, in 2014.

Starting in December 2014, he has been working as a doctoral student at Robert Bosch Gmbh, Tamm, Germany. During his work at Bosch, he has been working on inverter post-fault strategies for electric drives. Since 2018, he has been working at Valeo Siemens eAutomotive Germany Gmbh, Erlangen, as a System Simulation Engineer, where his focus is on electric drive system optimization.

Martin D. Hennen was born in Saarburg, Germany, in 1980. He received the Ph.D. degree in electrical engineering from RWTH Aachen University, Aachen, Germany, in 2012.

Starting in November 2005, he has been a Research Associate at the Institute for Power Electronics and Electrical Drives in Aachen, RWTH Aachen University. During his Ph.D. degree, he has been working on design, control, and fault tolerance of switched reluctance machines. Since 2012, he has been working at Robert Bosch GmbH, Stuttgart, Germany. His focus is on the system design of electrical drives for electric vehicle applications.

Antero Arkkio was born in Vehkalahti, Finland, in 1955. He received the M.Sc. (Tech.) and D.Sc. (Tech.) degrees from Helsinki University of Technology, Espoo, Finland, in 1980 and 1988, respectively.

He is currently an Emeritus Professor of Electrical Engineering with Aalto University, Espoo. His research interests include modeling, design, and measurement of electrical machines.

Anouar Belahcen, photograph and biography not available at the time of publication.